Bridging the translational gap: Implementation of multimodal small animal imaging strategies for tumor burden assessment in a co-clinical trial.

S.J. Blocker[1], Y.M. Mowery[2], M. D. Holbrook[1], Y. Qi[1], D.G. Kirsch[2,3], G.A. Johnson[1], C.T. Badea[1]*

[1]Center for In Vivo Microscopy, Duke University Medical Center, Durham, NC 27710

[2]Department of Radiation Oncology, Duke University Medical Center, Durham, NC, 27710

[3]Department of Pharmacology & Cancer Biology, Duke University Medical Center, Durham, NC, 27710

*Corresponding Author

Email: cristian.badea@duke.edu

Abstract

In designing co-clinical cancer studies, preclinical imaging brings unique challenges that emphasize the gap between man and mouse. Our group is developing quantitative imaging methods for the preclinical arm of a co-clinical trial studying immunotherapy and radiotherapy in a soft tissue sarcoma model. In line with treatment for patients enrolled in the clinical trial SU2C-SARC032, primary mouse sarcomas are imaged with multi-contrast micro-MRI (T1 weighted, T2 weighted, and T1 with contrast) before and after immune checkpoint inhibition and pre-operative radiation therapy. Similar to the patients, after surgery the mice will be screened for lung metastases with micro-CT using respiratory gating. A systems evaluation was undertaken to establish a quantitative baseline for both the MR and micro-CT systems against which others systems might be compared. We have constructed imaging protocols which provide clinically-relevant resolution and contrast in a genetically engineered mouse model of sarcoma. We have employed tools in 3D Slicer for semi-automated segmentation of both MR and micro-CT images to measure tumor volumes efficiently and reliably in a large number of animals. Assessment of tumor burden in the resulting images was precise, repeatable, and reproducible. Furthermore, we have implemented a publicly accessible platform for sharing imaging data collected during the study, as well as protocols, supporting information, and data analyses. In doing so, we aim to improve the clinical relevance of small animal imaging and begin establishing standards for preclinical imaging of tumors from the perspective of a co-clinical trial.

Introduction

The successful design and implementation of a cancer clinical trial faces many challenges, not the least of which is the translational relevance of related preclinical findings (1). While invaluable to cancer research, animal studies are typically completed before patient trials, effectively separating them from clinical observations and preventing bidirectional flow of information between the preclinical and clinical studies (2, 3). Further, preclinical protocols often fall short of mimicking clinical criteria, including schedule constraints and procedure time. To address such shortcomings, the implementation of co-clinical trials is of growing interest in cancer research (4, 5). Referring to the concerted execution of analogous animal and patient studies, co-clinical trials provide a setting in which clinical observations can influence the methodology used in animal experiments (6-8). In turn, novel findings from the preclinical arm can inform the patient study. In this way, co-clinical trials represent a strategy for dynamic integration of animal and patient studies to streamline cancer research efforts. However, the opportunity to lessen the translational divide offered by the co-clinical approach can be stifled by the complexities of designing a robust animal study. This is particularly true when considering the incorporation of small animal imaging into co-clinical studies of cancer.

Small animal imaging for co-clinical cancer trials represents an opportunity to simulate better clinical practice in animals (as imaging is often standard of care and essential for assessing disease response in clinical oncology), as well as to expand the information gathered during study. Technologies such as magnetic resonance (MR) can deliver

high-resolution images that describe tumor morphology and composition, as well as how tumors change over time or with treatment (9-11). Computed tomography (CT) provides an efficient, non-invasive method to detect new or metastatic lesions prior to development of symptoms (12, 13). The ability to non-invasively image animals at multiple time points greatly enhances the interpretation of tumor progression and/or therapeutic response, providing an avenue for comparison with longitudinal data from patients on study.

As with all translational research, care must be taken to reduce and acknowledge the differences between animal models and human cancer. Investigators must weigh factors such as tumor model selection, disease progression and intervention timelines, the immune condition of the animal, and the metabolic consequences of therapeutic interventions (2, 14, 15). Basing decisions on clinical standards and observations can promote the translation of findings between the arms of a co-clinical trial. However, the challenges that face translational imaging include both the biological and physical differences of the subjects and scanners, respectively.

While protocols for preclinical imaging are often designed with the intention of discovery, they routinely sacrifice efficiency and throughput for innovation (16). These scan programs are commonly project- and machine-specific, limiting their dissemination and broad employment. For example, a brief review of the literature discussing MR imaging in mice to measure tumor volume reveals a great deal of diversity among sequences, and acquisition parameters (Table I). By contrast, clinical scan protocols for tumor imaging are more standardized, achievable on a variety of systems, and typically limit scan durations for patient comfort and to accommodate scanner schedules.

Preclinical scanners must image at much higher resolution than clinical scanners, requiring different hardware solutions. Preclinical MR scanners employ smaller radio frequency coils and often operate at higher field strengths than clinical MR machines (3.0-11.0 T versus 1.5-3.0 T, respectively). The differences in image signal, resolution, artifacts, etc. must all be considered when designing animal imaging protocols to serve a co-clinical trial (17, 18). Thus, the disparity between preclinical and clinical cancer imaging makes correlation of results challenging, potentially reducing the impact and utility of preclinical imaging.

With these challenges in mind we sought to identify clinically-applicable scan protocols to measure tumor burden in a genetically engineered mouse model (GEMM) of soft tissue sarcoma. Specifically, the co-clinical trial requires reproducible detection of changes in primary tumor volume with MR after therapeutic intervention, with follow up detection and measurement of lung metastases with CT. Our goal was to produce images that were comparable to scans performed in an ongoing clinical trial of sarcoma (NCT03092323), while establishing protocols for acquisition, data processing, and image analysis that are reproducible and broadly relevant. These protocols are currently being employed in an ongoing co-clinical trial to assess the effects of neoadjuvant and adjuvant programmed cell death protein 1 (PD-1) inhibition in sarcomas treated with neoadjuvant radiation therapy and surgical resection (19) (see Fig 1). Finally, we have established a resource for public dissemination of preclinical imaging data, protocols, and results. In doing so, we have developed a robust blueprint for incorporating clinically-driven mouse imaging into a co-clinical trial, and a pipeline to promote rigorous reporting and sharing of preclinical imaging practices.

Table I. Samples found in the literature on preclinical MR sequences for solid tumor volume measurements in mice

	Sequence	Field Strength (T)	TE (ms)	TR (ms)	Slice Thickness (mm)	NEX	In-plane resolution (mm^2)	Acquisition time	Ref(s)
T1-Weighted Images	Spin Echo (SE)	7	12.5 to 17	750 to 500	1.0-2.0	NR	0.125 to 0.130	NR	(20, 21)
	Fast Spin Echo (FSE)	9.4	7	1800 to 2500	1.00	10.0 to 12.0	0.195 to 0.234	5m 53s to 6m 45s	(22)
	Gradient Recalled Echo (GRE)	11.7	3	436.5	0.60	2	0.117	6m to 9m	(23)
	Multi-echo GRE (MGE)	9.4	2.5 to 11.5	225	0.70	3	0.1	NR	(24)
T2-Weighted Images	Spin Echo (SE)	4.7 to 9.4	10.8 to 60.0	1000 to 4000	0.42 to 2	1 to 4	0.117 to 0.313	9 m (or NR)	(25-28)
	Fast Spin Echo (FSE, MSFSE)	1.0 to 9.4	19.0 to 48.0	1000 to 5500	0.75 to 2	2	0.156 to 0.220	9m to 25 m	(21, 29-32)
	Fast Recovery Fast Spin Echo (FRFSE)	1.5	85	2200	1.20	3	0.243	NR	(32)
	Turbo Spin Echo (TSE)	1.5 to 7	13.0 to 80.0	480 to 4400	0.562 to 2	1 to 4	0.111 to 0.2	3m 35s to 5m 54s (or NR)	(33-37)
	Gradient Recalled Echo (GRE)	1.5 to 9.4	1.0 to 9.0	3.6 to 50	0.71 to 0.128	2 to 10	0.128 to 0.156	3m 48s (or NR)	(38-40)
	Rapid Acquisition with Relaxation Enhancement (RARE)	1.5 to 14	4.5 to 36.0	890 to 5000	0.5 to 1	2 to 4	0.098 to 0.234	57s (or NR)	(24, 41-44)

TE: Echo time
TR: Repetition time
MS: Multi-slice
NEX: Averages
m: minutes, s: seconds
NR: "not reported," indicating that one or more reference did not report the specified parameter.

Materials and methods

GEMM of inducible sarcoma

To mimic the clinical presentation and progression of human sarcomas with gradual tumor development and metastasis in the setting of an intact immune system, a carcinogen-induced GEMM of sarcoma (Lee CL, Mowery YM, Daniel AR, et all, submitted) was chosen for the animal studies of the co-clinical trial. Primary sarcomas (*p53*/MCA model) are generated by intramuscular delivery into the gastrocnemius of adenovirus expressing Cre recombinase (Adeno-Cre; Gene Transfer Vector Core, University of Iowa) into $p53^{fl/fl}$ mice followed by intramuscular injection of 0.3 mg 3-methylcholanthrene (MCA; Sigma-Aldrich, Saint Louis, MO) at the same site. Tumors develop approximately 8-12 weeks after induction. Imaging studies were initiated when tumors were palpable (>100 mm^3), as well as at various stages of disease progression.

Small animal MR imaging at 7T

All MR experiments were performed on a 7.0 T Bruker Biospec small animal MRI scanner (Bruker Inc., Billerica, MA). In preliminary experiments three commercial Bruker radiofrequency (RF) coils were explored: i) a 72 mm diameter actively decoupled linear volume coil for transmission and reception (Bruker #: T10720V3); ii) a 35 mm diameter quadrature volume coil for transmission and reception (Bruker #: T9988V3); iii) a mouse brain receive-only four coil array (Bruker #: T11765V3), combined with the 72 mm volume coil for transmission. Scan acquisition was performed using ParaVision®

6.0.1 platform (Bruker Inc.), and the reconstructed images were stored in DICOM format.

MR System Baseline Performance

A systems evaluation was undertaken to establish a quantitative baseline for our MR system against which others systems might be compared. First, a cylindrical phantom (62 mm diameter, 120 mm length) containing a 3D-printed grid of 1.0 mm squares was scanned with the 72 mm volume coil to measure linearity and geometric distortions across the active volume of the scanner. A second scan was performed of an 18mm x 18 mm cylindrical water bottle filled with 10 M $CuSO_4$ to measure B0 homogeneity across the field of view. These data were stored for periodic Quality Assurance (QA) checks during the protocol.

To provide guidance on design of a T1/T2 phantom, a mouse bearing a primary soft tissue sarcoma of the hind limb was scanned in the 72 mm volume coil to obtain T1 and T2 maps across the tumor. The volume coil was used to provide uniform B1 excitation to facilitate accurate T1/T2 mapping. The lower sensitivity of this coil was offset by increasing the number of averages and slice thickness (NEX = 2; Slice Thickness = 1.0 mm). T1 maps were acquired using Multi-Slice Multi-Echo (MSME) sequences with variable TR (TR = 3200 ms, 1600 ms, 800 ms, 400 ms, 200 ms, 100 ms, 50 ms, and 25 ms). T2 maps were acquired using multi-gradient echo (MGE) sequences with variable TE (TE = 10 ms, 20 ms, 30 ms…200 ms). T1 and T2 fitting was performed on the series using ImageJ open-source software (https://imagej.nih.gov/ij/), and a range of T1 and T2 values measured in the tumor were defined. Tumor-applicable T1 values were

used to generate a contrast dilution series of gadopentetate dimeglumine (Gd-DTPA; Magnevist®, Bayer HealthCare Pharmaceuticals, Wayne, NJ) in distilled water. T2 values in the tumor were mimicked with a series of agarose concentrations.

Based on observed T1 and T2 values in the tumor, tubes containing a range of Gd-DTPA and agarose concentrations were assembled into a 3D-printed, custom phantom (subsequently referred to as the "study phantom"). A resolution insert was designed for integration into the study phantom which contained laser-cut holes in a 0.5 x 6.0 mm diameter Cirlex disk with holes ranging from 200-75 μm in diameter. The study phantom was loaded with the contrast series and resolution insert, and enclosed in a 20 ml syringe, through which water was pulled and air removed. The phantom was scanned with the surface coil using the described scan protocol (Table II) to assess contrast delineation and spatial resolution. Finally, the bias field of the surface coil array was evaluated by scanning a tube of distilled water and the study phantom. Post-acquisition bias corrections were assessed with the study phantom by placing it in a coil-affixed tube where it was laterally constrained but free to rotate. The coil was positioned and the study phantom was scanned with a series of 2D T1-weighted sequences using the protocol developed for the animal studies. After each scan the phantom was rotated 10-15 degrees. These scans were used to quantitatively measure the efficacy of the bias corrections used in the post-processing pipeline to remove the radiofrequency (rf) sensitivity bias in the 4-element surface coil used for the study.

Mouse MR image acquisition

All animal handling and imaging procedures were performed according to protocols approved by the Duke Institutional Animal Care and Use Committee (IACUC). Tumor images were acquired using the 4-element surface coil array (receive) coupled with the 72 mm linear volume (transmit) coil. Anesthesia was induced with an isoflurane suspension administered on cotton gauze in a contained chamber, followed by maintenance via inhaled isoflurane in concentrations of 1-2% in air. Mice were placed in a left lateral recumbent position on a custom 3D-printed bed equipped with warm water circulation (between 35-40°C) and respiratory rate monitoring. The tumor bearing limb was positioned beneath the surface coil, which was fastened to the coil platform of the bed to reduce displacement. The entire bed platform was positioned within the magnet and mice were monitored for the duration of scanning, with isoflurane concentration adjusted as needed to maintain steady breathing. T1 contrast enhancement was performed by injection of 0.5 mmol/kg Gd-DTPA via tail vein catheter which was placed under anesthesia prior to scanning. Injection speed was 2.5 ml/min, and contrast was allowed to circulate for 3 minutes to achieve peak enhancement. Upon completion, catheters were removed, and mice were returned to warmed cages for anesthesia recovery (<5 minutes).

A systematic comparison of sequences and parameters was undertaken to yield a protocol with T1 and T2 contrast analogous to the clinical trial. Spatial resolution was scaled appropriately for the mouse and tradeoffs between scan parameters balanced to provide signal to noise comparable to the clinical scan in a realistic scan time. The final sequence selections are outlined in Table III. Briefly, the scan protocol was developed which contained a T1-weighted and T2-weighted sequence, followed by repeat of the

T1 sequence after Gd-DTPA injection. Upon positioning a mouse in the magnet, routine adjustments were performed, including wobble and shims. Including a 3-minute wait period for circulation of contrast agent post-injection, the entire scan program lasted 40 minutes and 27 seconds for each mouse, plus approximately 5 minutes for initial placement, alignment and adjustments.

In vivo tumor volume assessment with MR

Volume measurement of tumors imaged with MR was performed with multiple methods to assess accuracy, precision, reproducibility, and inter-user variance. T2-weighted images (as described in Table III) were used in refining and testing volume calculation methods. Slice-by-slice, hand-drawn segmentation was used as the "gold standard" for volume determination, with initial segmentations performed in triplicate to determine user precision. Hand-drawn segmentations were executed in the 2D Viewer platform of OsiriX DICOM viewing software version 9.0.2 (Pixmeo Sarl, Bernex, Switzerland).

Semi-automated tumor segmentation was also explored and refined in 3D Slicer (https://www.slicer.org), an open-source software developed as part of the National Alliance for Medical Image Computing (NA-MIC) under the NIH. Tumors were segmented with a modified protocol for image adjustment and automatic volume propagation. Briefly, DICOM images obtained with the surface coil array were subjected to a bias correction to compensate for signal fall-off which occurs at increasing distances from the coil surface. Bias correction was performed under the N4ITK MRI Bias Correction module in 3D Slicer (45) using the T1-weighted image without contrast as a mask, and the resulting bias-corrected T2 images were used for

segmentation. Volume propagation was performed by defining regions of tumor, as well as surrounding non-tumor tissues, on one slice of each orthogonal view near the center of the lesion with the paintbrush editor. Following planar region of interest (ROI) definition, the "GrowCut" tool was used to grow the 3D volume of interest (VOI) considered to be a tumor (46), and the resulting volumes were refined with the "Remove Islands" tool. Semi-automated segmentation was performed in triplicate and results were compared to hand-drawn volumes.

Micro-CT imaging

All micro-CT imaging was performed using a micro-CT system developed in house (47). Free breathing animals were scanned under anesthesia using 2–3% isoflurane delivered by nose-cone. A pneumatic pillow positioned on the thorax was connected to a pressure transducer to monitor breathing and for respiratory gating. Body temperature was maintained with heat lamps and a feedback controller. Scan parameters were 80 kVp, 40 mA, 10 ms/exposure. A total of 360 views were acquired over a 360° rotation. The reconstruction was performed with a 63 um isotropic voxel size using Feldkamp algorithm (48) followed by bilateral filtration (49) to reduce noise. The micro-CT images were converted to Hounsfield units (HU) and saved as DICOM files. The radiation dose associated with a micro-CT scan was ~0.017 Gy per mouse. This is ~294 to 411 times less than LD50/30 lethal dose (5-7 Gy) in mice (50).

Phantom examinations for CT

To assess image quality, a commercially available performance evaluation micro-CT phantom (www.simutec.com) was imaged. The phantom (model vmCT 610) incorporates six plates, each of which is designed to evaluate different aspects of micro-CT image quality with a single scan. These include CT number calibration, CT number linearity, image noise, image uniformity, spatial resolution, geometric accuracy.

Micro-CT acquisition using prospective respiratory gating

Unlike in clinical chest CT, which is performed in a single breath hold, preclinical projection data in micro-CT must be acquired over many breaths, requiring respiratory gating. Respiratory gating can be performed prospectively or retrospectively (51). In prospective respiratory gating, a single respiratory phase (e.g. end-expiration) can serve well to assess lung nodules. We were first to develop and implement combined cardiac and respiratory gating for micro-CT (52), which provides the highest possible cardio-pulmonary imaging quality. But for this preclinical study focused on assessing lung metastases longitudinally in a large number of mice, adding cardiac gating substantially increases acquisition times and was considered not essential. Consequently, we have used prospective gating to synchronize acquisition with respiration only using a respiratory signal provided by a pneumatic pillow positioned on the chest of the animal. In prospective gating, the acquisition of each projection is triggered when the respiratory signal crosses above a user-defined threshold. Thus, all projections are acquired in the same part of the respiratory cycle e.g. in end-inspiration, minimizing motion artifacts and blurring in the reconstructions.

To assess the performance of our gated lung tumor imaging, we used mice with primary lung cancer. Lung tumors were generated by intranasal injection of Adeno-Cre into LSL-*Kras*^{G12D}; *p53*$^{fl/fl}$ mice (53, 54). Mice were imaged at 12 weeks post Adeno-Cre infection, at which point multiple primary lung tumors (~0.5–1.5 mm in diameter) were detectable within each mouse. Each mouse was scanned three times *in vivo* with and without gating. A post-mortem scan was also performed for each mouse and deemed the gold standard for lesion sizes. The lung tumors were semi-automatically segmented using 3D Slicer with the GrowCut tool as previously described for MR images. Volumes were calculated three times per condition, which included a non-gated *in vivo* image, a gated *in vivo* image, and a post-mortem image acquired (standard).

Development of web-accessible archives for protocol and data dissemination

The Center for In Vivo Microscopy (CIVM) at Duke has initiated a novel approach to sharing data in all of our publications through the use of VoxPort/VoxStation. This integrated package was developed under National Cancer Institute (NCI) support (CA088658) specifically for project management of this nature. VoxPort is a MYSQL database that provides the user with tools for capture and upload of a wide range of data types: IACUC protocols, imaging and set up protocols, 2, 3 and 4D images (more than 30 different formats) from multiple sources (MRI,CT, conventional histology) and data analysis (Excel, graphics, etc). Voxport annotates and organizes these data for efficient search and review by an external user. VoxStation, the companion software,

277 provides external users interactive access to data without requiring download of large,
278 unnecessary files.

279 Statistical analysis

280 Reliability and repeatability of volume measurements were assessed using one-way
281 ANOVA as well as by calculating coefficients of variance, where $p<0.05$ was considered
282 statistically significant. Differences in output measurements were compared with the
283 student's t-test, where $p<0.05$ was considered statistically significant. Precision of
284 repeated measures were interpreted via Brown-Forsythe testing. Statistical analyses
285 were performed and visualized using GraphPad Prism version 7.00 for Mac (GraphPad
286 Software, La Jolla California, US).

Results

Establishment of a preclinical protocol for volume measurement of primary sarcomas

Our primary objective was to define a preclinical MR protocol that provided spatial resolution and contrast differential comparable to that of the clinical arm of the trial. To make the protocol practical it must replicate the three acquisitions used in the clinical arm i.e. T1 weighted, T2 weighted, and T1 with contrasts (Fig 1). The final constraint placed on the protocol was that it had to be executed in < 1 hr. Since the mouse is ~ 3000 times smaller than the human, the spatial resolution should be scaled comparably. The spatial resolution in the human protocol (Supporting Table 1) is 1.0 x 2.0 x 5.0 mm i.e. voxels of 10 mm^3. Thus, our target resolution (voxel volume) is 0.003 mm^3. The exceptional contrast of MR becomes important in sarcoma lesions receiving RT, as the volume of responding tumors may temporarily increase due to tissue damage and edema, possibly resulting in false assumptions of progression (55, 56). Both T1 and T2 contrast in MR are dependent of the magnetic field as T1 increases and T2 decreases with field (57). Clinical studies are performed at 1.5-3.0 T. This preclinical arm is performed at 7.0 T, so TR and TE have been adjusted iteratively within the rest of the constraints of the protocol to achieve contrast differences between tumor and muscle that are comparable to the clinical arm.

Fig 1. Schematic representation of a co-clinical trial which utilizes translational imaging. Flow charts describing the clinical (A) and preclinical (B) sections of a co-clinical trial of RT with or without the addition of PD-1 inhibition in soft tissue sarcoma. Treatment dosing and imaging procedures in the preclinical arm have been designed to mimic the clinical trial as closely as possible.

Table II shows the sensitivity and homogeneity for a uniform 18 mm diameter water bottle scanned using the three different rf coil configurations: 72 mm volume coil, transmit receive; 35 mm volume coil, transmit receive; 72 mm volume coil transmit, 4-element surface coil receive. The relative sensitivity of the two volume coils is well defined, with demonstrated homogeneity superior to the surface coil. However, the approximately 3-fold higher sensitivity of the surface coil provides a compelling argument for its use, as desirable SNR is achievable with relatively short scan times. The 5-fold increase in variance of image intensity when using the surface coil is attributable to location-dependent bias. Placement of the surface coil directly onto the tumor-bearing limb reduces the distance between the coil and tumor tissues, somewhat reducing the effect of inhomogeneity in identifying lesions. However, the remaining bias is able to be addressed with the employment of a bias correction (see Fig 4).

Table II. Sensitivity and homogeneity of a uniform sample scanned with three rf coil configurations for small animal MR at 7.0T

	72mm Volume Coil		35mm Volume Coil		Quadrature Surface Coil + 72mm Volume Coil	
	T1	T2	T1	T2	T1	T2
SNR	4.83	4.78	6.76	6.86	17.16	17.32
Coefficient of Variance	18.1%	16.8%	12.4%	12.1%	75.6%	72.2%

3D isotropic imaging is frequently employed in preclinical imaging to provide signal averaging required for the smaller voxels. Clinical MR protocols use 2D (anisotropic) multi-slice sequences to maintain practical scan times. We compared both 2D anisotropic and 3D isotropic sequences in sarcoma-bearing limbs. The contrast to noise ratio and scan times are shown for several variations in (Supporting Fig 1). 2D sequences for T1-weighted and T2-weighted images with 100 um in-plane (axial) resolution and slice thickness of 300 μm were achievable with 3 NEX with short acquisition times (~10 minutes and ~15 minutes, respectively). Further, these images were acquired over a field of view (FOV) sufficient to cover any tumor imaged on study.

In following the direction of the clinical MR program, a T1-weighted and T2-weighted sequence was selected, with T1-acquisition performed without and with injection of contrast. A time course of short T1-weighted acquisitions was performed to identify peak contrast time in tumor tissues (Supporting Fig. 2). The resulting sequences were incorporated into an MR scan protocol suitable for clinically-relevant imaging of primary soft tissue sarcoma lesions of the hind leg for purposes of longitudinal tumor volume assessment (Table III). A comparison of clinical MR images of a patient with a sarcoma

in the leg and a tumor-bearing mouse hind limb is shown in Fig 2. Importantly, the clinically-driven preclinical protocol is achievable in less than one hour providing the efficiency necessary for a large study.

Table III. Clinically-driven scan program for preclinical MR imaging of soft tissue sarcomas of the extremity

Sequence	Protocol	Acquisition Parameters		Image Geometry		Time
T1-Weighted	T1_FLASH	TE	4.5 ms	FOV	28 mm X 28 mm	09m : 44s
		TR	925.486 ms	Matrix	280 X 280	
		Averages	3	Resolution	100 µm	
		Flip angle	30°	Slice thickness	300 µm	
				Slice number	60	
T2-Weighted	T2_TurboRARE	TE	45 ms	FOV	28 mm X 28 mm	14m : 59s
		TR	8563.193 ms	Matrix	280 X 280	
		Averages	3	Resolution	100 µm	
		RARE	8	Slice thickness	300 µm	
				Slice number	60	
T1-Weighted + Contrast	T1_FLASH	TE	4.5 ms	FOV	28 mm X 28 mm	03m : 00s + 09m : 44s
		TR	925.486 ms	Matrix	280 X 280	
		Averages	3	Resolution	100 µm	
		Flip angle	30°	Slice thickness	300 µm	
		Start delay	3 min. post-inj.	Slice number	60	
					Total	**37m : 27s**

TE: Echo time
TR: Repetition time

Fig 2. Comparison of human and mouse MR images acquired for the co-clinical trial. Micro-MR images of a sarcoma-bearing mouse leg (bottom row) were obtained with a scan program designed to mimic images acquired in patients enrolled in the clinical arm (top row) bearing soft tissue sarcomas of the extremity. T1-weighted (left), T2-weighted (middle), and T1-weighted + contrast agent injection (right) were acquired

in both the human and the mouse arms of the co-clinical trial. White scale bars indicate distances of 5 mm.

Phantom scans for qualification of preclinical MR systems in achieving a clinically-relevant scan program

Baseline studies were performed as part of a standard quality assurance protocol and validation of scanner performance which served as the preclinical equivalent of standard clinical QA. These protocols were performed regularly throughout study to ensure scanner performance. Scanner linearity, rf coil homogeneity, and magnetic field homogeneity are demonstrated in Supporting Figs 3 and 4, respectively.

Since high-resolution and tissue contrast were the driving motivations for sarcoma imaging with MR, a project-focused “study phantom” was designed to ensure that selected protocols were adequate for tumor volume measurements. To address tissue contrast, T1 and T2 mapping of an established sarcoma were calculated to identify a range of T1 and T2 values which will likely be encountered in tumors on study (Supporting Fig. 5). To mimic contrasts that span the range of tumor-associated T1 values, a series dilution of magnevist was generated. Syringes containing multiple dilutions of magnevist in water were placed in a holder, and T1 mapping was performed to determine the concentration-dependent T1 values. Solutions which produced T1 values within the range present in tumor tissues were selected for incorporation into the study phantom (Fig 3, top). Similarly, a series of agarose concentrations were scanned to determine T2 values, and solutions mimicking T2 values seen in the tumor were

372 selected for phantom construction (Fig 3, bottom). The constructed study phantom was
373 used to confirm the utility of the selected rf coils and scan protocols for successful tumor
374 detection and volume measurement (Fig 4).

375

376 **Fig 3. T1 and T2 fitting across a preclinical soft tissue sarcoma demonstrate the**
377 **anticipated T1 signal range of tumors on study.** Histograms of T1 (A), and T2 (D)
378 values measured in sarcoma tissues are shown, including the mean (blue line) and 2
379 standard deviations (shaded light blue). Bottles containing a dilution series of
380 magnevist (B) and agarose (E) were measured in the 72 mm volume coil and used to
381 mimic the ranges of T1 and T2 values in tumor during construction of a custom study
382 phantom. Linear regressions of T1 or T2 measurements (C and F, respectively) were
383 plotted along a log scale of solution concentration and shown with 95% CI (dotted lines).

384

385 **Fig 4. A custom study phantom demonstrates T1 + T2 range and resolution for**
386 **mouse sarcoma imaging.** A 3D-printed phantom was designed to hold tubes
387 containing a range of magnevist (T1) and agarose (T2) concentrations, as well as a
388 resolution insert, and was loaded into a syringe filled with water (A). The T1 sequence
389 used in the preclinical trial demonstrates the range of T1 signal within predetermined
390 magnevist concentrations (B), where dilution factor refers to the dilution of a 1% solution
391 in deionized water. The T2 sequence used in the preclinical trial demonstrates the
392 range of T2 signal within predetermined agarose gel concentrations (C). The resolution

393 insert confirms sufficient resolution of the sequences down to 100um (D). Images
394 shown have not been altered or corrected for bias.

395 Evaluation and correction of image biases present during
396 high-field MR imaging

397 When operating at higher fields, artifacts may appear that are not seen or are negligible
398 in clinical scans. One of the most notable of these inconsistencies is the introduction or
399 amplification of biases in the resulting images. At 7.0 T, the rf wavelength approaches
400 dimensions of the area of interest being imaged, often leading to an area of unexpected
401 brightness in the image center (58-60). This effect, attributed to dielectric resonance,
402 was measured using two uniform phantoms: a 30 ml syringe filled with 10 mM $CuSO_4$
403 and one filled with silicon oil (Supporting Fig. 5). T1-weighted and T2-weighted
404 sequences (defined in Table I) both demonstrated measurable central brightening
405 across the $CuSO_4$ phantom, an effect not appearing in the silicon oil (58). Thus, we
406 identified dielectric resonance as a source of bias in the resulting mouse images.

407 An independent and more obvious bias exists in image intensity as a function of
408 distance from the surface coil itself. The spatial (B1) sensitivity of the multi-coil is a
409 widely recognized bias that is exacerbated at high field strengths. The resulting shifts in
410 signal intensity can confound tumor detection and measurement, particularly in deep-
411 seated tissues. To overcome this issue, we identified the best parameters with which to
412 implement N4ITK bias correction in the study images using 3D Slicer (45, 61). Further
413 improvement of the bias correction was achieved by using a contrast-reduced T1 image

(TE = 4.5 ms; TR = 3000 ms), which reflected only the spatial bias, as a weighted filter during correction. Original T1-weighted images of the study phantom demonstrate the overwhelming effect of the surface coil spatial bias, where magnevist concentration dependence is degraded based on distance from the coil surface (Fig 5 A, left). However, application of filtered bias correction (Fig 5 A, right) resulted in restoration of magnevist concentration-dependence in the T1 image signal (Fig 5 B). This served as rationale for application of a bias correction to T2-weighted images on which tumor volumes would be calculated due to better contrast. The scan program includes a T1-weighted image without contrast injection which provides little contrast of use in defining tumor at 7.0 T. However, this can be employed for weighted filtering of the refined N4ITK bias correction, which was subsequently applied to images to improve tumor volume analysis.

Fig 5. Correction of position-dependent bias resulting from use of the surface coil. A custom phantom containing concentrations of magnevist with T1 values that span those anticipated in tumors were scanned using the surface coil. T1-weighted imaging of the phantom demonstrated a significant bias (A, left), which distorted the intensity of the magnevist tubes due to distance from the coil. Resulting measurements were unable to reflect the concentration-dependent signal appropriately (B). Application of an N4ITK bias correction, masked with a proton density weighted image (TR = 3000) reduced the effects of the coil bias (A, right), restoring linearity in the signal vs concentration curve (B).

MR scans with the quadrature surface coil deliver reliable and repeatable volume estimates despite repositioning of tumor-bearing limbs

With the goal of reliable tumor volume measurement, images acquired with the clinically-driven MR scan protocol were used to determine its practical utility. First, reliability of scans for volume measurements was tested by scanning tumor-bearing limbs three times in succession with repositioning using the same scan program (Fig 6 A). In each of three scanned mice with morphologically distinct tumors, calculated volumes did not differ based on leg position (Fig 6 C-D). Further, no significant difference in measurement precision was observed in any scan position (Fig 6 E). These data suggest that employment of the clinically-driven MR scan protocol was repeatable and reproducible, regardless of tumor position or orientation beneath the surface coil.

Fig 6. Reliability and consistency of tumor volume measurements in repeated scans with limb repositioning. T2-weighted images were analyzed to determine reproducibility of tumor volume measurements resulting from three consecutive scans of sarcoma-bearing limbs in three positions. Each mouse was scanned three times in succession, with the tumor-bearing limb positioned under the surface coil in a flexed, relaxed, or extended position to shift the location and shape of the tumor (represented as blue in the diagram shown in (A)). ROIs were hand-drawn slice-by-slice in triplicate

in each resulting image (9 total measurements per mouse) (B), and calculated volumes were compared for repeatability (user precision) and reproducibility (consistency with shifting position) (C). ANOVA analysis of volume reproducibility suggested no dependence of volume measurements on leg position (D), and precision of hand-drawn measurements was confirmed using Brown-Forsythe (E).

Semi-automated tumor segmentation demonstrates similar accuracy and precision to hand-drawn measurements of tumor volume, with reasonable inter-user variance

With the inclusion of an advanced bias correction, we have employed tools in 3D Slicer for semi-automated segmentation of T2-weighted MR images to measure tumor volumes efficiently and reliably in a large number of animals. Semi-automated segmentation was compared to volumes calculated with hand-drawn ROIs ("gold-standard") in T2-weighted tumor images corrected for bias (Fig 7 A and B). ANOVA of the resulting tumor volumes revealed no significant difference in calculated volumes or precision between methods (Fig 7 C). Further, when both techniques were applied to 6 independent tumor image samples, Bland-Altman analysis confirmed reasonable agreement between segmentation methods (Fig 7 D). Taken together these data suggest that volumes calculated by applying a bias correction and subsequent semi-automated tumor segmentation in 3D Slicer are comparable to results from hand-drawn analyses. For studies with large animal numbers, this is very advantageous, as the semi-automated segmentation protocol usually requires <5 minutes to complete.

Fig 7. Semi-automated tumor segmentation with 3D Slicer is an acceptable alternative to hand-drawn ROIs for sarcoma volume measurement. T2-weighted images of three tumors of varying size and morphology were analyzed with hand-drawn ROIs and semi-automated segmentation to calculate tumor volume. Examples of hand-drawn (A) and semi-automated (B) segmentation of the same tumor are shown, including an axial slice of the segmented tumor (a.) and the rendered 3D representation of the tumor according to each segmentation (b.). Resulting volume calculations were compared between triplicate measures with each method for each tumor (C), demonstrating similar measurements and comparable precision. Bland-Altman analysis of both methods, when employed in 6 separate tumors, indicated that semi-automated segmentation is a viable alternative to hand-drawn segmentation.

Employment of respiratory gating during micro-CT acquisition improved tumor burden assessment in lung tissues

Baseline studies were performed as part of a standard quality assurance protocol and validation of scanner performance which served as the preclinical equivalent of standard clinical QA. These protocols were performed regularly throughout study to ensure scanner performance. Spatial resolution, geometric accuracy, iodine concentration measurement, and uniformity were all assessed (Supporting Fig 6).

498 During a non-gated micro-CT (Fig 8 A), lung motion often causes blurred tissue
499 boundaries, particularly along the lung wall or near the diaphragm (Fig 8C). Respiratory
500 gating (Fig 8 B) improves the ability to identify small tumors and discern borders
501 between tissues in contact (Fig 8 D).

502

503 **Fig 8. Prospective gating allows for synchronization of image acquisition with**
504 **breathing patterns.** Micro-CT acquisition monitoring without (A) and with respiratory
505 gating (B). Coronal images of a lung tumor are shown without gating (C), with
506 respiratory gating (D), and post-mortem (E). Tumor is indicated by white arrows, and
507 diaphragm is noted with yellow arrows. Representative images from triplicates are
508 shown.

509 A collection of tumors was selected for identification and volume measurement in each
510 of the 9 acquired images (3 non-gated, 3 respiratory-gated, and 3 post-mortem scans).
511 Selected tumors varied in size and location with diverse surrounding structures (Fig 9A).
512 Mean volume measurements of tumors in respiratory-gated images more closely
513 reflected values measured in post-mortem images than did non-gated tumor
514 measurements. One-way ANOVA of measurements collected for each tumor showed
515 that half of the samples demonstrated significant differences in output values in non-
516 gated images when compared to post-mortem samples (Fig 9B and C). Further, better
517 precision was observed in gated analyses than non-gated analyses (Fig 9D). Taken
518 together, these data support that respiratory gating reduces effects of breathing motion
519 in both the accuracy and precision of lung tumor volume measurements.

Fig 9. Respiratory gating improves precision and accuracy of lung tumor volume assessment in a free-breathing mouse. Multiple tumors of varying size and location in the lungs of a free-breathing mouse scanned with micro-CT were identified (A, a-d). Hand-drawn ROIs were used to calculate the volume of each lesion in each scan (a total of 9 measurements per tumor). ANOVA showed that in half of the lesions, respiratory gating had a significant impact on the accuracy of volume measurement (B and C). Variance within repeated measures from gated images was approximately double that of post-mortem images, while non-gated image results demonstrated more than five-fold variance compared to post-mortem measurements (D).

Databases constructed via VoxPort allow users web-access to co-clinical animal imaging data, acquisition and analysis protocols, and supporting materials

This integrated package was developed under NCI support (CA088658) specifically for project management of this nature. VoxPort is a MYSQL database that provides the user tools for capture and upload of a wide range of data types: IACUC, imaging and set up protocols, 2,3 and 4D images (more than 30 different formats), from multiple sources (MRI,CT, conventional histology) and data analysis (Excel, graphics, etc). Voxport annotates and organizes these data so an external user can efficiently search and review. VoxStation, the companion software, provides external users interactive access to all these data without need to download vast troves of what might be useless.

Fig 10 illustrates Voxport/Voxstation in action displaying both images and protocols. Access to our Voxport Image Management System is available at: https://civmvoxport.vm.duke.edu/voxbase/index.php . The visitor will be prompted to login to CIVMVoxPort using the provided credentials (User Name: DukeU24, Password: DukeU24Review)".

Fig 10. Demonstration of the VoxPort interface for image data sharing. Images of VoxPort demonstrating archives of multiple forms of imaging data, including images from multiple modalities, protocol documentation and standard operating procedures, scan acquisition information, and segmentation stacks which correspond to archived images. The image gallery provides a thumbnail and metadata about the images. The user can choose to download a given image or stack or examine the data within the interface.

Discussion

In order to bridge the gap between preclinical and clinical research, care must be taken to develop animal models and imaging protocols that appropriately reflect the clinical question. To serve a co-clinical study of PD-1 inhibition for sarcoma, we have described the establishment, qualification, and application of preclinical MRI and CT imaging protocols for longitudinal assessment of therapeutic efficacy in a GEMM of soft tissue sarcoma. The imaging protocols are clinically-driven, reproducible, suitable for high-throughput studies, and readily extended to experiments using different tumor models or interventions.

In selecting micro-MRI protocols, we gained higher spatial resolution (100 μm in-plane) by using a quadrature surface coil placed over the tumor-bearing limbs of animals. We assembled a scan program to generate images similar to those acquired in the clinic (T1-weighed, T2-weighed, and T1-weighted plus contrast) with spatial resolution scaled for the size of the mouse, contrast comparable to the clinical arm of the study, and total acquisition time lasting less than 1 hour. With this program, tumor volume measurements were reliable regardless of tumor size or depth, and independent of shifts in the tumor orientation/position beneath the coil.

Similar to the clinic, periodic imaging of mouse lung tissues following treatment and resection of primary sarcomas is being used to monitor metastatic development. The principal challenge in assessing tumor burden in the lungs with micro-CT is the effect of respiratory motion on resulting images. We have employed respiratory gating techniques to mitigate the effects of motion by limiting acquisition to defined periods in

576 the breathing cycle. Tissue barriers, such as diaphragm, lung wall, and tumors
577 boundaries, were visibly more clear in gated images compared to images acquired
578 throughout the full breathing cycle. As a result, tumor volume measurements from
579 gated images more accurately matched post-mortem standards and demonstrated
580 improved precision compared to measurements from non-gated images, improving
581 tumor burden assessment.

582 Finally, we have created a web accessible repository to store and share these
583 protocols, representative data, supporting studies (e.g. pathology, blood chemistry). In
584 sharing our findings over the course of the study, we hope to assist others in generating
585 and evaluating their preclinical and co-clinical imaging studies. Overall, we have
586 devised a strategy for incorporation of preclinical imaging into a co-clinical trial for the
587 evaluation of tumor burden, as well as established a means by which to efficiently
588 organize and share the resulting data.

Conclusions

We have established a routine pipeline by which high-volume preclinical imaging data can support and inform in real time a co-clinical trial of combined RT and immunotherapy in sarcoma. Additionally, we have outlined a blueprint for navigating and overcoming some of the technical challenges that translational tumor imaging studies face. The resulting methods are both clinically-relevant and widely adaptable. Although the field of animal imaging lacks standards of practice and reporting, we have generated a means by which our data, protocols, and processing methods can be accessed and used as a template by others. By establishing clinically-driven preclinical imaging methods to serve in a co-clinical trial, we have created a pipeline which reduces the gap between preclinical and clinical studies of sarcoma therapy.

Acknowledgements

All small animal imaging work was performed at the Duke Center for In Vivo Microscopy. We thank Lixia Liu and Nerissa Williams with assistance with caring for mice.

References

1. Ledford H. Translational research: 4 ways to fix the clinical trial. Nature. 2011;477(7366):526-8.

2. Ruggeri BA, Camp F, Miknyoczki S. Animal models of disease: pre-clinical animal models of cancer and their applications and utility in drug discovery. Biochem Pharmacol. 2014;87(1):150-61.

3. Wartha K, Herting F, Hasmann M. Fit-for purpose use of mouse models to improve predictivity of cancer therapeutics evaluation. Pharmacol Ther. 2014;142(3):351-61.

4. Clohessy JG, Pandolfi PP. Mouse hospital and co-clinical trial project--from bench to bedside. Nat Rev Clin Oncol. 2015;12(8):491-8.

5. Lunardi A, Pandolfi PP. A co-clinical platform to accelerate cancer treatment optimization. Trends Mol Med. 2015;21(1):1-5.

6. Chen Z, Cheng K, Walton Z, Wang Y, Ebi H, Shimamura T, et al. A murine lung cancer co-clinical trial identifies genetic modifiers of therapeutic response. Nature. 2012;483(7391):613-7.

7. Nardella C, Lunardi A, Patnaik A, Cantley LC, Pandolfi PP. The APL paradigm and the "co-clinical trial" project. Cancer Discov. 2011;1(2):108-16.

8. Nishino M, Sacher AG, Gandhi L, Chen Z, Akbay E, Fedorov A, et al. Co-clinical quantitative tumor volume imaging in ALK-rearranged NSCLC treated with crizotinib. Eur J Radiol. 2017;88:15-20.

9. Haris M, Yadav SK, Rizwan A, Singh A, Wang E, Hariharan H, et al. Molecular magnetic resonance imaging in cancer. J Transl Med. 2015;13:313.

630 10. Kauppinen RA, Peet AC. Using magnetic resonance imaging and spectroscopy
631 in cancer diagnostics and monitoring: preclinical and clinical approaches. Cancer Biol
632 Ther. 2011;12(8):665-79.
633 11. Lin G, Keshari KR, Park JM. Cancer Metabolism and Tumor Heterogeneity:
634 Imaging Perspectives Using MR Imaging and Spectroscopy. Contrast Media Mol
635 Imaging. 2017;2017:6053879.
636 12. Clark DP, Lee CL, Kirsch DG, Badea CT. Spectrotemporal CT data acquisition
637 and reconstruction at low dose. Med Phys. 2015;42(11):6317-36.
638 13. Li XF, Zanzonico P, Ling CC, O'Donoghue J. Visualization of experimental lung
639 and bone metastases in live nude mice by X-ray micro-computed tomography. Technol
640 Cancer Res Treat. 2006;5(2):147-55.
641 14. Day CP, Merlino G, Van Dyke T. Preclinical mouse cancer models: a maze of
642 opportunities and challenges. Cell. 2015;163(1):39-53.
643 15. Le Magnen C, Dutta A, Abate-Shen C. Optimizing mouse models for precision
644 cancer prevention. Nat Rev Cancer. 2016;16(3):187-96.
645 16. O'Connor JPB. Cancer heterogeneity and imaging. Semin Cell Dev Biol.
646 2017;64:48-57.
647 17. Bokacheva L, Ackerstaff E, LeKaye HC, Zakian K, Koutcher JA. High-field small
648 animal magnetic resonance oncology studies. Phys Med Biol. 2014;59(2):R65-R127.
649 18. Gillies RJ, Bhujwalla ZM, Evelhoch J, Garwood M, Neeman M, Robinson SP, et
650 al. Applications of magnetic resonance in model systems: tumor biology and physiology.
651 Neoplasia. 2000;2(1-2):139-51.

19. Mowery YM, Ballman KV, Riedel RF, Brigman BE, Attia S, Meyer CF, et al. SU2C-SARC032: A phase II randomized controlled trial of neoadjuvant pembrolizumab with radiotherapy and adjuvant pembrolizumab for high-risk soft tissue sarcoma. Journal of Clinical Oncology. 2018;36(15_suppl):TPS11588-TPS.

20. Fite BZ, Wong A, Liu Y, Mahakian LM, Tam SM, Aina O, et al. Magnetic resonance imaging assessment of effective ablated volume following high intensity focused ultrasound. PLoS One. 2015;10(3):e0120037.

21. Vormoor B, Knizia HK, Batey MA, Almeida GS, Wilson I, Dildey P, et al. Development of a preclinical orthotopic xenograft model of ewing sarcoma and other human malignant bone disease using advanced in vivo imaging. PLoS One. 2014;9(1):e85128.

22. Sapi J, Kovacs L, Drexler DA, Kocsis P, Gajari D, Sapi Z. Tumor Volume Estimation and Quasi-Continuous Administration for Most Effective Bevacizumab Therapy. PLoS One. 2015;10(11):e0142190.

23. Jimenez-Gonzalez M, Plaza-Garcia S, Arizeta J, Bianchessi S, Trigueros C, Reese T. A longitudinal MRI study on lymph nodes histiocytosis of a xenograft cancer model. PLoS One. 2017;12(7):e0181043.

24. Linxweiler J, Korbel C, Muller A, Jungel E, Blaheta R, Heinzelmann J, et al. Experimental imaging in orthotopic renal cell carcinoma xenograft models: comparative evaluation of high-resolution 3D ultrasonography, in-vivo micro-CT and 9.4T MRI. Sci Rep. 2017;7(1):14249.

673 25. Hectors SJ, Jacobs I, Strijkers GJ, Nicolay K. Multiparametric MRI analysis for
674 the identification of high intensity focused ultrasound-treated tumor tissue. PLoS One.
675 2014;9(6):e99936.
676 26. Jeon TY, Kim CK, Kim JH, Im GH, Park BK, Lee JH. Assessment of early
677 therapeutic response to sorafenib in renal cell carcinoma xenografts by dynamic
678 contrast-enhanced and diffusion-weighted MR imaging. Br J Radiol.
679 2015;88(1053):20150163.
680 27. Kersemans V, Cornelissen B, Allen PD, Beech JS, Smart SC. Subcutaneous
681 tumor volume measurement in the awake, manually restrained mouse using MRI. J
682 Magn Reson Imaging. 2013;37(6):1499-504.
683 28. Larkin TJ, Canuto HC, Kettunen MI, Booth TC, Hu DE, Krishnan AS, et al.
684 Analysis of image heterogeneity using 2D Minkowski functionals detects tumor
685 responses to treatment. Magn Reson Med. 2014;71(1):402-10.
686 29. Ramasawmy R, Johnson SP, Roberts TA, Stuckey DJ, David AL, Pedley RB, et
687 al. Monitoring the Growth of an Orthotopic Tumour Xenograft Model: Multi-Modal
688 Imaging Assessment with Benchtop MRI (1T), High-Field MRI (9.4T), Ultrasound and
689 Bioluminescence. PLoS One. 2016;11(5):e0156162.
690 30. Whisenant JG, Sorace AG, McIntyre JO, Kang H, Sanchez V, Loveless ME, et al.
691 Evaluating treatment response using DW-MRI and DCE-MRI in trastuzumab responsive
692 and resistant HER2-overexpressing human breast cancer xenografts. Transl Oncol.
693 2014;7(6):768-79.

694 31. Zhang F, Cao J, Chen X, Yang K, Zhu L, Fu G, et al. Noninvasive Dynamic
695 Imaging of Tumor Early Response to Nanoparticle-mediated Photothermal Therapy.
696 Theranostics. 2015;5(12):1444-55.
697 32. Zhang P, Wang B, Chen X, Cvetkovic D, Chen L, Lang J, et al. Local Tumor
698 Control and Normal Tissue Toxicity of Pulsed Low-Dose Rate Radiotherapy for
699 Recurrent Lung Cancer: An In Vivo Animal Study. Dose Response.
700 2015;13(2):1559325815588507.
701 33. Almeida GS, Panek R, Hallsworth A, Webber H, Papaevangelou E, Boult JK, et
702 al. Pre-clinical imaging of transgenic mouse models of neuroblastoma using a dedicated
703 3-element solenoid coil on a clinical 3T platform. Br J Cancer. 2017;117(6):791-800.
704 34. Bagci U, Kramer-Marek G, Mollura DJ. Automated computer quantification of
705 breast cancer in small-animal models using PET-guided MR image co-segmentation.
706 EJNMMI Res. 2013;3(1):49.
707 35. Liebsch L, Kailayangiri S, Beck L, Altvater B, Koch R, Dierkes C, et al. Ewing
708 sarcoma dissemination and response to T-cell therapy in mice assessed by whole-body
709 magnetic resonance imaging. Br J Cancer. 2013;109(3):658-66.
710 36. Rajendran R, Huang W, Tang AM, Liang JM, Choo S, Reese T, et al. Early
711 detection of antiangiogenic treatment responses in a mouse xenograft tumor model
712 using quantitative perfusion MRI. Cancer Med. 2014;3(1):47-60.
713 37. Yang SH, Lin J, Lu F, Han ZH, Fu CX, Lv P, et al. Evaluation of antiangiogenic
714 and antiproliferative effects of sorafenib by sequential histology and intravoxel
715 incoherent motion diffusion-weighted imaging in an orthotopic hepatocellular carcinoma
716 xenograft model. J Magn Reson Imaging. 2017;45(1):270-80.

717 38. Blasiak B, Landry J, Tyson R, Sharp J, Iqbal U, Abulrob A, et al. Molecular
718 susceptibility weighted imaging of the glioma rim in a mouse model. J Neurosci
719 Methods. 2014;226:132-8.
720 39. Dassler K, Scholle FD, Schutz G. Dynamic gadobutrol-enhanced MRI predicts
721 early response to antivascular but not to antiproliferation therapy in a mouse xenograft
722 model. Magn Reson Med. 2014;71(5):1826-33.
723 40. Muller A, Jagoda P, Fries P, Graber S, Bals R, Buecker A, et al. Three-
724 dimensional ultrashort echo time MRI and Short T2 images generated from subtraction
725 for determination of tumor burden in lung cancer: Preclinical investigation in transgenic
726 mice. Magn Reson Med. 2018;79(2):1052-60.
727 41. Beloueche-Babari M, Jamin Y, Arunan V, Walker-Samuel S, Revill M, Smith PD,
728 et al. Acute tumour response to the MEK1/2 inhibitor selumetinib (AZD6244, ARRY-
729 142886) evaluated by non-invasive diffusion-weighted MRI. Br J Cancer.
730 2013;109(6):1562-9.
731 42. Mustafi D, Fernandez S, Markiewicz E, Fan X, Zamora M, Mueller J, et al. MRI
732 reveals increased tumorigenesis following high fat feeding in a mouse model of triple-
733 negative breast cancer. NMR Biomed. 2017;30(10).
734 43. Song Y, Cho G, Suh JY, Lee CK, Kim YR, Kim YJ, et al. Dynamic contrast-
735 enhanced MRI for monitoring antiangiogenic treatment: determination of accurate and
736 reliable perfusion parameters in a longitudinal study of a mouse xenograft model.
737 Korean J Radiol. 2013;14(4):589-96.

738 44. Zhang T, Zhang F, Meng Y, Wang H, Le T, Wei B, et al. Diffusion-weighted MRI
739 monitoring of pancreatic cancer response to radiofrequency heat-enhanced intratumor
740 chemotherapy. NMR Biomed. 2013;26(12):1762-7.
741 45. Tustison NJ, Avants BB, Cook PA, Zheng Y, Egan A, Yushkevich PA, et al.
742 N4ITK: improved N3 bias correction. IEEE Trans Med Imaging. 2010;29(6):1310-20.
743 46. Vezhnevets V, Konouchine V. Growcut: Interactive multi-label N–D image
744 segmentation by cellular automata. Proc GraphiCon. 2005:7.
745 47. Badea C, Johnston S, Johnson B, De Lin M, Hedlund LW, Johnson GA. A Dual
746 Micro-CT System for Small Animal Imaging SPIE, Medical Imaging; San Diego, CA:
747 SPIE; 2008.
748 48. Feldkamp LA, Davis LC, Kress JW. Practical cone-beam algorithm. J Opt Soc
749 Am. 1984;1(6):612-19.
750 49. Tomasi C, Manduchi R. Bilateral filtering for gray and color images. Proc of the
751 1998 IEEE International Conference on Computer Vision. 1998:839-46.
752 50. Carlson SK, Classic KL, Bender CE, Russell SJ. Small animal absorbed radiation
753 dose from serial micro-computed tomography imaging. Mol Imaging Biol. 2007;9(2):78-
754 82.
755 51. Badea C, Drangova M, Holdsworth D, Johnson G. In vivo small-animal imaging
756 using micro-CT and digital subtraction angiography. Phys Med Biol. 2008;53:R319.
757 52. Badea CT, Hedlund LW, Johnson GA. Micro-CT with respiratory and cardiac
758 gating. Medical Physics. 2004;31(12):3324-9.

759 53. Johnson L, Mercer K, Greenbaum D, Bronson RT, Crowley D, Tuveson DA, et al.
760 Somatic activation of the K-ras oncogene causes early onset lung cancer in mice.
761 Nature. 2001;410(6832):1111-6.
762 54. Kirsch DG, Grimm J, Guimaraes AR, Wojtkiewicz GR, Perez BA, Santiago PM,
763 et al. Imaging primary lung cancers in mice to study radiation biology. Int J Radiat Oncol
764 Biol Phys. 2010;76(4):973-7.
765 55. Cuneo KC, Mito JK, Javid MP, Ferrer JM, Kim Y, Lee WD, et al. Imaging primary
766 mouse sarcomas after radiation therapy using cathepsin-activatable fluorescent imaging
767 agents. Int J Radiat Oncol Biol Phys. 2013;86(1):136-42.
768 56. Messiou C, Bonvalot S, Gronchi A, Vanel D, Meyer M, Robinson P, et al.
769 Evaluation of response after pre-operative radiotherapy in soft tissue sarcomas; the
770 European Organisation for Research and Treatment of Cancer-Soft Tissue and Bone
771 Sarcoma Group (EORTC-STBSG) and Imaging Group recommendations for
772 radiological examination and reporting with an emphasis on magnetic resonance
773 imaging. Eur J Cancer. 2016;56:37-44.
774 57. Johnson GA, Herfkens RJ, Brown MA. Tissue relaxation time: in vivo field
775 dependence. Radiology. 1985;156(3):805-10.
776 58. Bernstein MA, Huston J, 3rd, Ward HA. Imaging artifacts at 3.0T. J Magn Reson
777 Imaging. 2006;24(4):735-46.
778 59. Collins CM, Liu W, Schreiber W, Yang QX, Smith MB. Central brightening due to
779 constructive interference with, without, and despite dielectric resonance. J Magn Reson
780 Imaging. 2005;21(2):192-6.

781 60. Hoult DI, Phil D. Sensitivity and power deposition in a high-field imaging
782 experiment. J Magn Reson Imaging. 2000;12(1):46-67.
783 61. Fedorov A, Tuncali K, Fennessy FM, Tokuda J, Hata N, Wells WM, et al. Image
784 registration for targeted MRI-guided transperineal prostate biopsy. J Magn Reson
785 Imaging. 2012;36(4):987-92.
786
787

Supporting information

S1 Table. Comparison of imaging parameters between the clinical and preclinical arms of the co-clinical trial.

S1 Figure. 2D tumor imaging achieves adequate signal with reduced acquisition time compared to 3D acquisition. T2-weighted images of a primary sarcoma lesion of the hind limb were acquired with both 2D (A) and 3D (B) TurboRARE sequences. TE was fixed at 45 ms, and both resulting images had an in-plane resolution of 100um (C). Signal in both images was adequate for deciphering tumor location and boundaries at 1 NEX, but the acquisition time to generate the 3D image was more than 7X that of the 2D acquisition. Reduced scan time of the 2D sequence allows time for incorporation of multiple NEX while maintaining a clinically-relevant scan program length.

S2 Figure. Magnevist contrast enhancement peaks at approximately 6 minutes post-injection. A series of short (~ 1 min) T1 FLASH sequences in the hind limb of a tumor-bearing mouse were performed before, during, and after injection of magnevist. Time course images (A) were obtained to determine wash-in, peak, and wash out of contrast in tumor compared to baseline (B). The highest intensity of contrast in tumor was observed approximately 6 minutes following injection. Subsequent scan programs

808 included a delay between injection and scan initiation to align peak contrast within the
809 acquisition window of the T1 protocol.

810

811 **S3 Figure. Scanner linearity and rf coil homogeneity.** A large, custom-printed 3D
812 grid phantom comprised of 1 mm rods in 10mM $CuSO_4$ was used to demonstrate
813 scanner linearity over the area in which the surface coil is employed (A). Surface coil
814 operation occurs within the defined yellow box. To measure homogeneity, a uniform
815 bottle containing distilled water was scanned with the 72 mm volume coil (B) and the
816 surface coil operating in the 72 mm coil (C), and signal was plotted as a function of
817 distance over the volume of the bottle.

818

819 **S4 Figure. Identification of image bias due to dielectric effects measured in**
820 **images acquired with the 72 mm volume coil.** To measure the influence of the
821 dielectric effect in images acquired using the 72 mm volume coil, images of 30 ml
822 bottles containing 10mM $CuSO_4$ in deionized water (A.a.) and Silicone Oil (A.b.) were
823 acquired with the volume coil (transceiver; independent of the surface coil). A linear
824 region of interest with a width of 20 pixels (yellow box) was used to measure signal
825 intensity across the diameter of the bottle. Signal intensity shifts due to the dielectric
826 effect are measurable across the diameter of the $CuSO_4$ water bottle (B.a.), and are not
827 present in images of Silicone Oil (B.b.).

828

829 **S5 Figure. T1 and T2 maps of sarcoma tumors provide anticipated T1 and T2**
830 **values of tumor tissues.** T1 and T2 maps were acquired over multiple slices of an
831 established sarcoma of the hind limb. A T2-weighted TurboRARE sequence was used
832 to delineate tumor ROIs (A). Tumor tissue and anatomical landmarks are indicated (T =
833 tumor; Bl = bladder; S = spine). The tumor ROI used to measure contrast is shown on
834 the T1 map (B) and T2 map (C).

835

836 **S6 Figure. Optimization and calibration of the microCT.** Demonstration of the
837 selected phantom (A) as well as image quality evaluation results of micro-CT scans are
838 shown. An axial micro-CT slice thorough the spatial resolution plate with the 4 coils of
839 alternating aluminum and Mylar sheets demonstrate measured layer thicknesses of 50,
840 100, 150, and 200 μm corresponding to 10, 5, 3.3, and 2.5 line pairs per mm (lp/mm),
841 respectively (B). Only the first 2 coils show spatial frequencies that can be separated,
842 indicating image resolution around 3.3 lp/mm. The phantom contains a geometric
843 accuracy plate which includes two peripheral beads and a central bead. The two
844 measured distances are reasonably similar to the ones indicated by the manufacturer,
845 with an error around 50 μm. This error is under one pixel size value of 63μm (C). A plot
846 of the measured CT number versus known iodine concentration (D.a.; yellow rings)
847 demonstrates a significant linear correlation between signal intensity and increasing
848 iodine concentration (D.b.). A line profile (D.a.; red line) confirms uniformity with relative

849 variations less than 11 % across the field of view without significant cupping artifacts

850 due to beam hardening (D.c.).

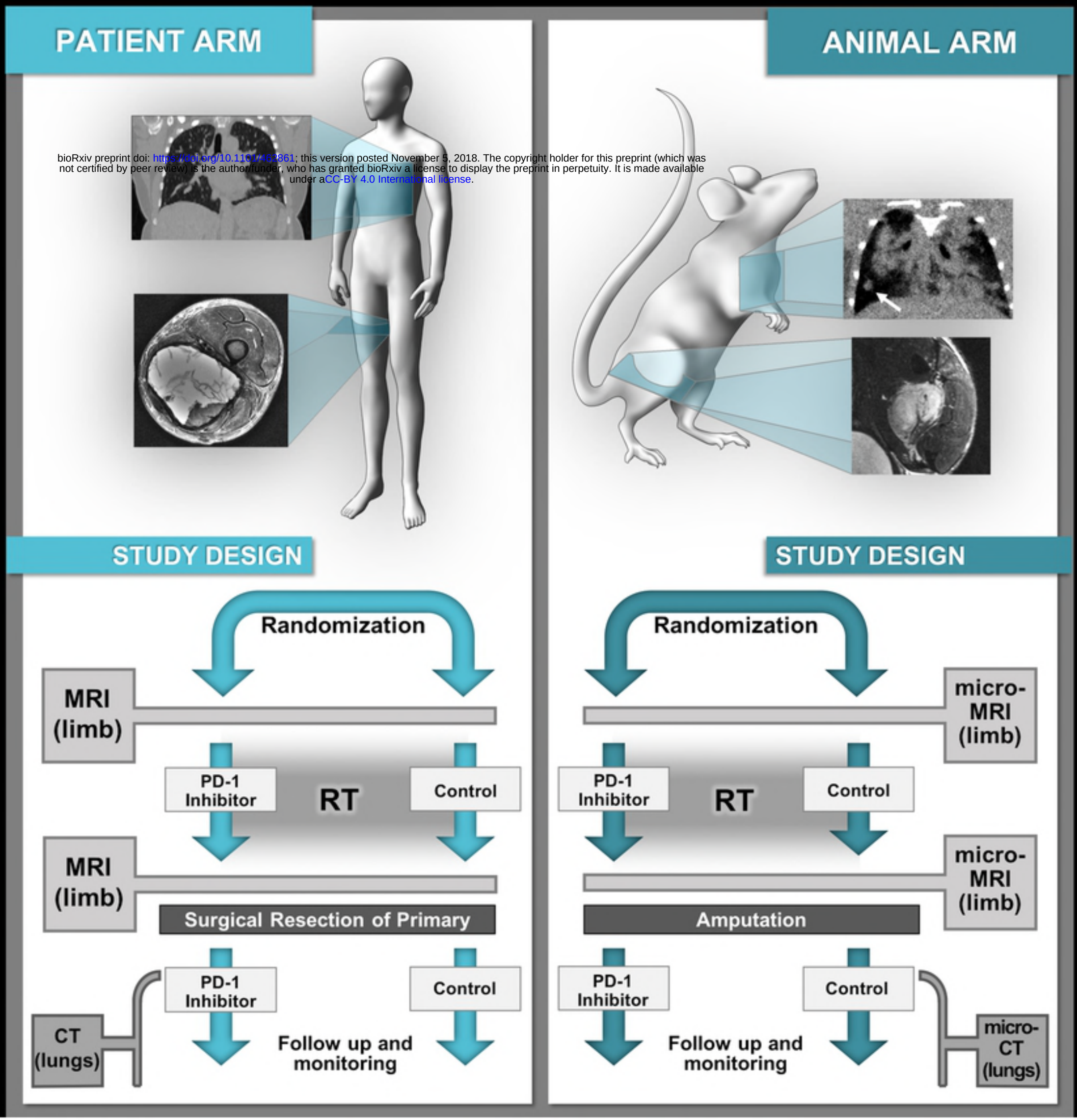

Fig 1

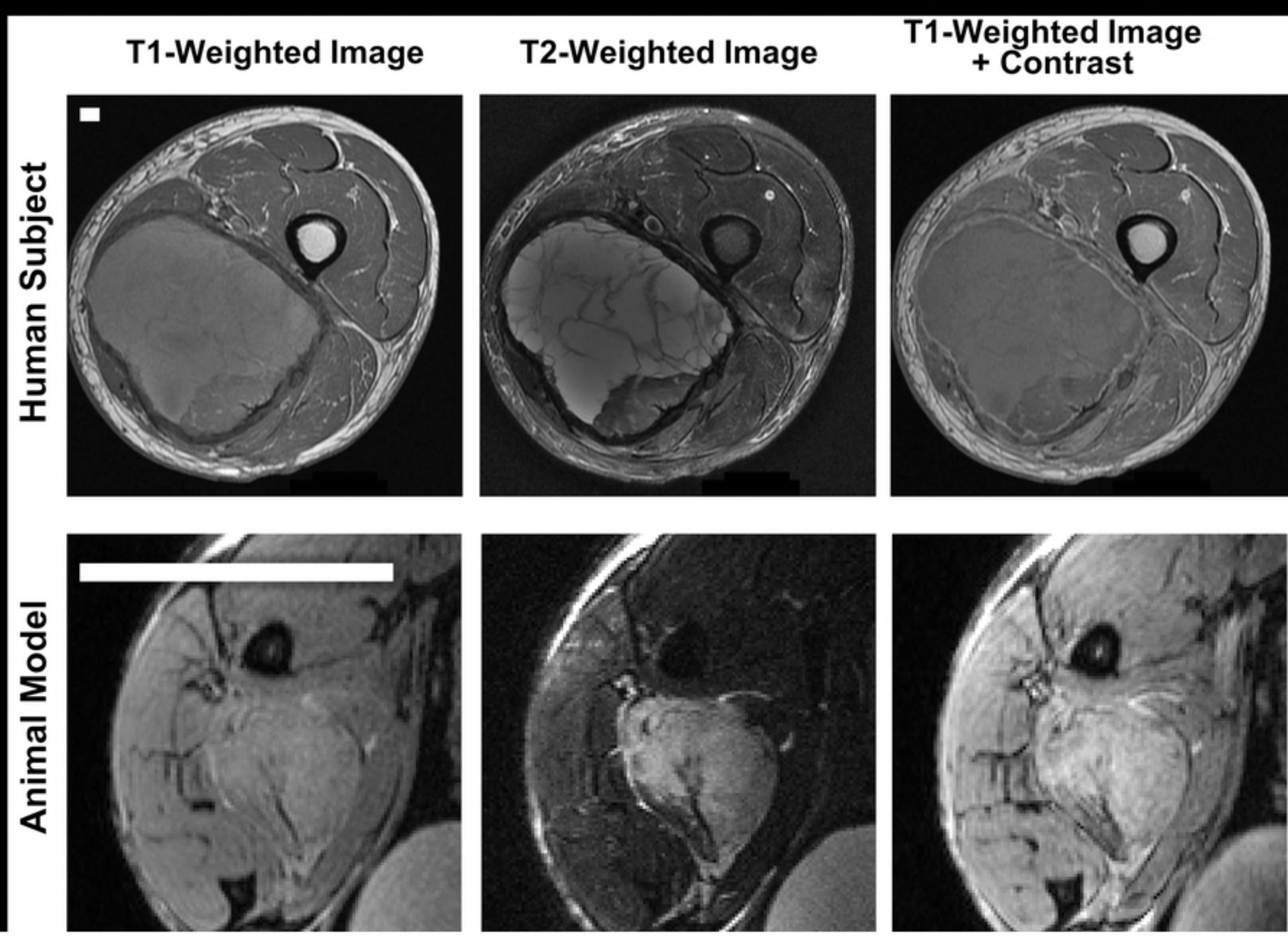
T1-Weighted Image
T2-Weighted Image
T1-Weighted Image + Contrast
Human Subject
Animal Model

Fig 2

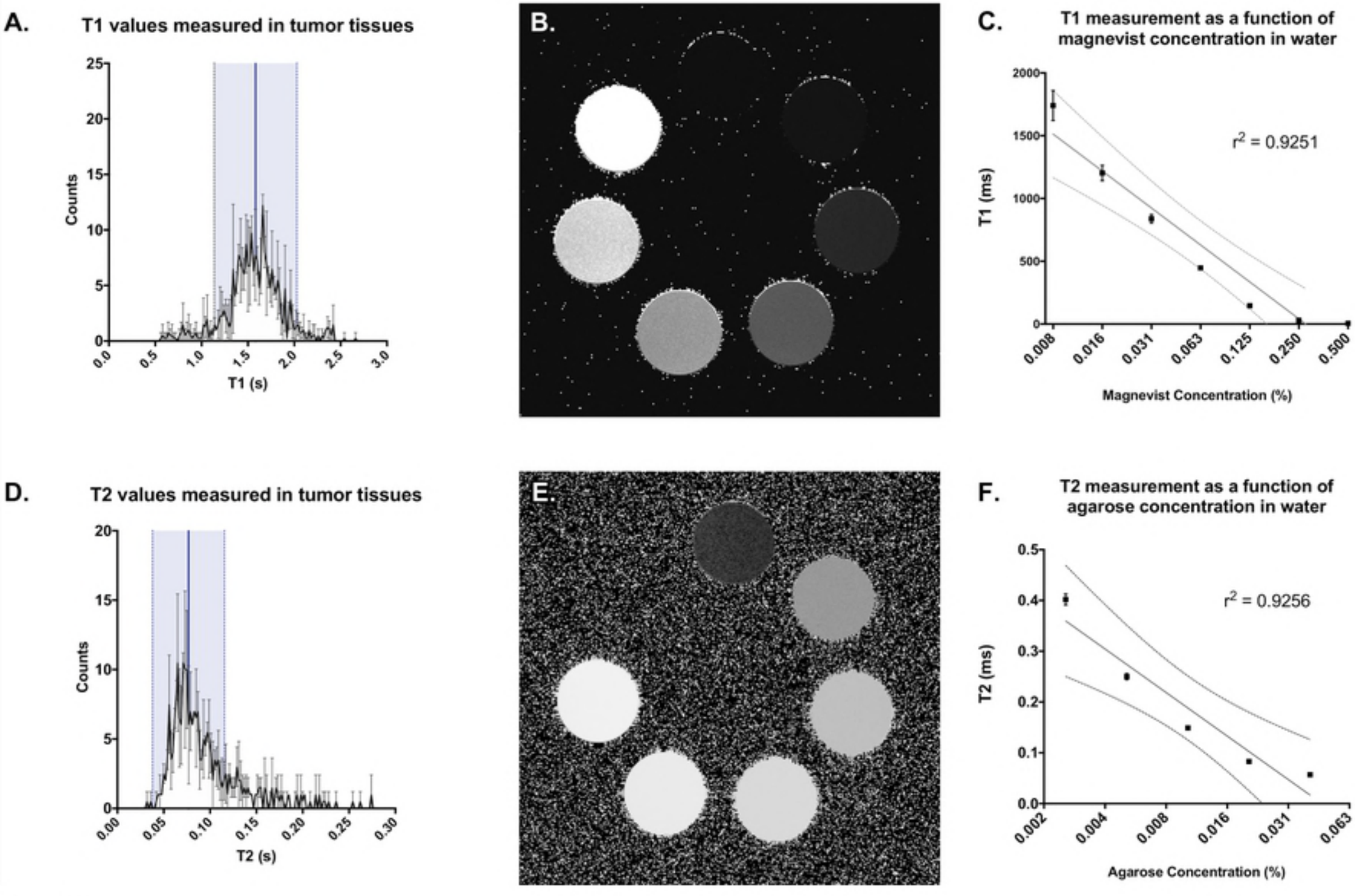
A.
T1 values measured in tumor tissues
Counts
T1 (s)
B.
C.
T1 measurement as a function of magnevist concentration in water
T1 (ms)
r^2 = 0.9251
Magnevist Concentration (%)
D.
T2 values measured in tumor tissues
Counts
T2 (s)
E.
F.
T2 measurement as a function of agarose concentration in water
T2 (ms)
r^2 = 0.9256
Agarose Concentration (%)

Fig 3

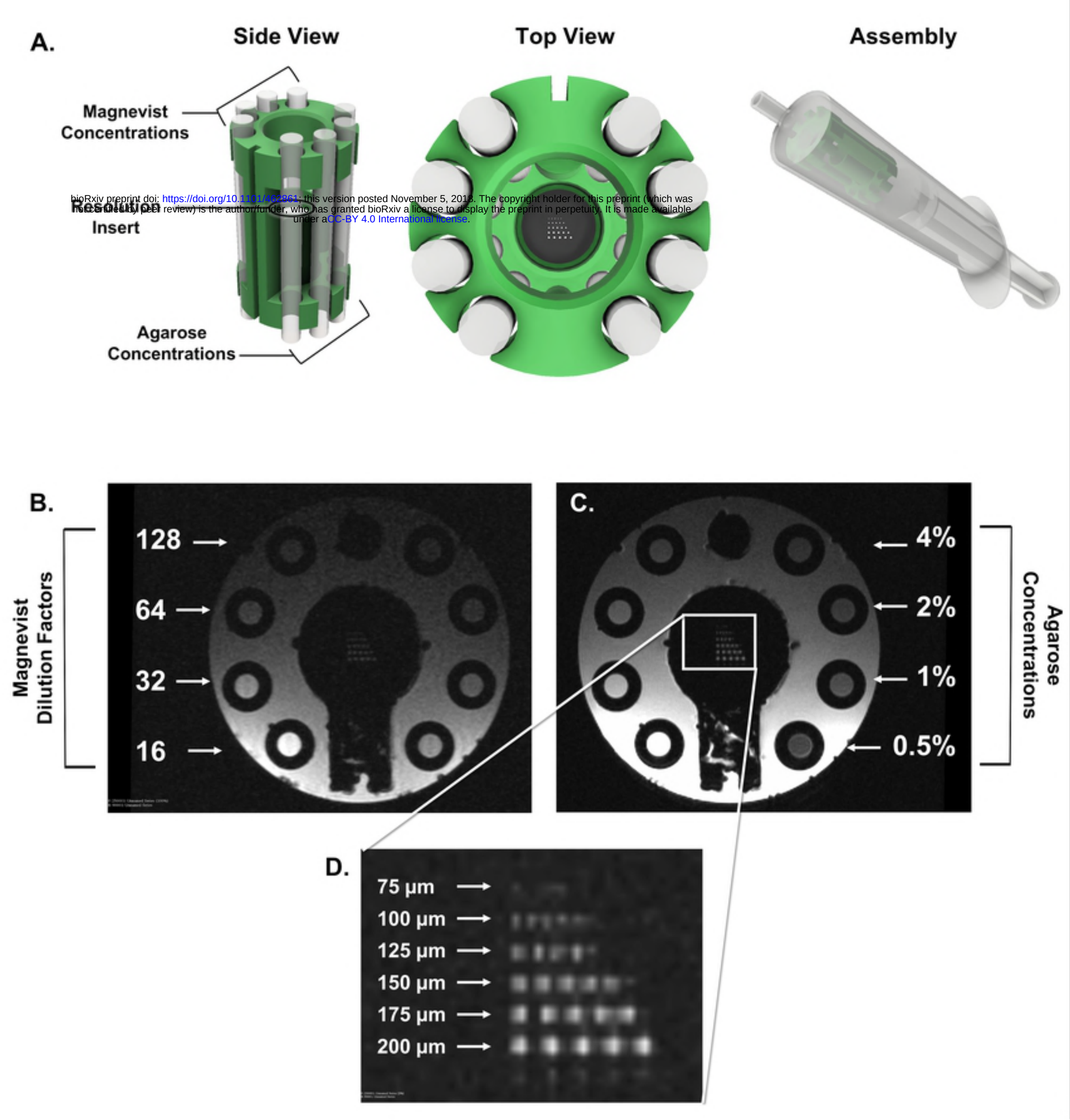

Fig 4

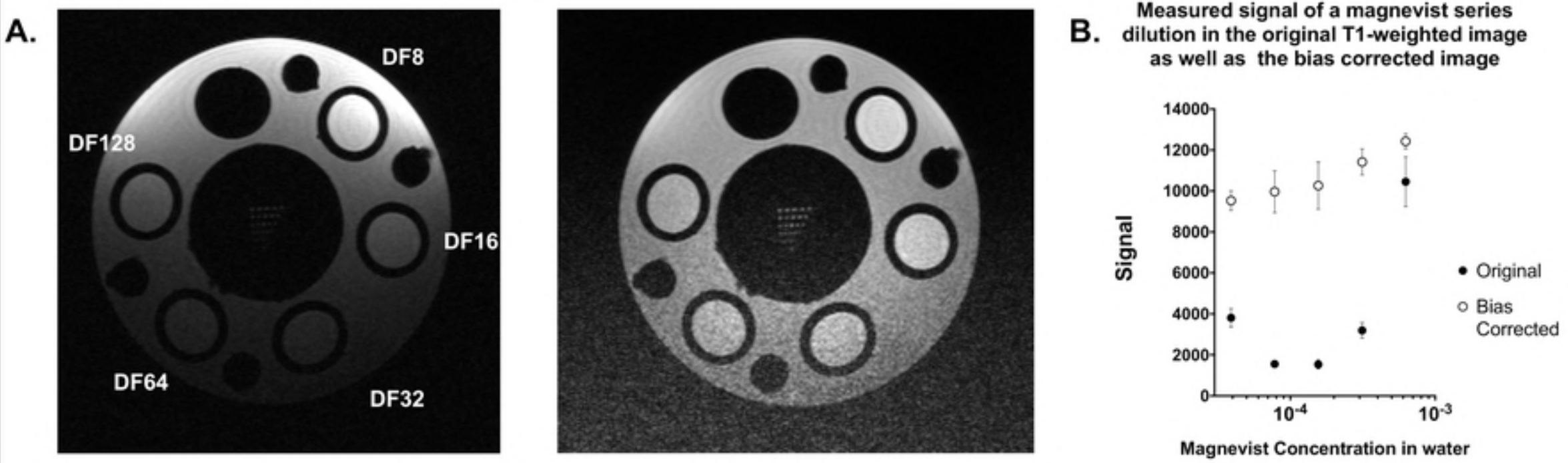
A.
DF8
DF128
DF16
DF64
DF32
B.
Measured signal of a magnevist series dilution in the original T1-weighted image as well as the bias corrected image
Signal
14000
12000
10000
8000
6000
4000
2000
0
10^{-4}
10^{-3}
Original
Bias Corrected
Magnevist Concentration in water

Fig 5

A.

B.

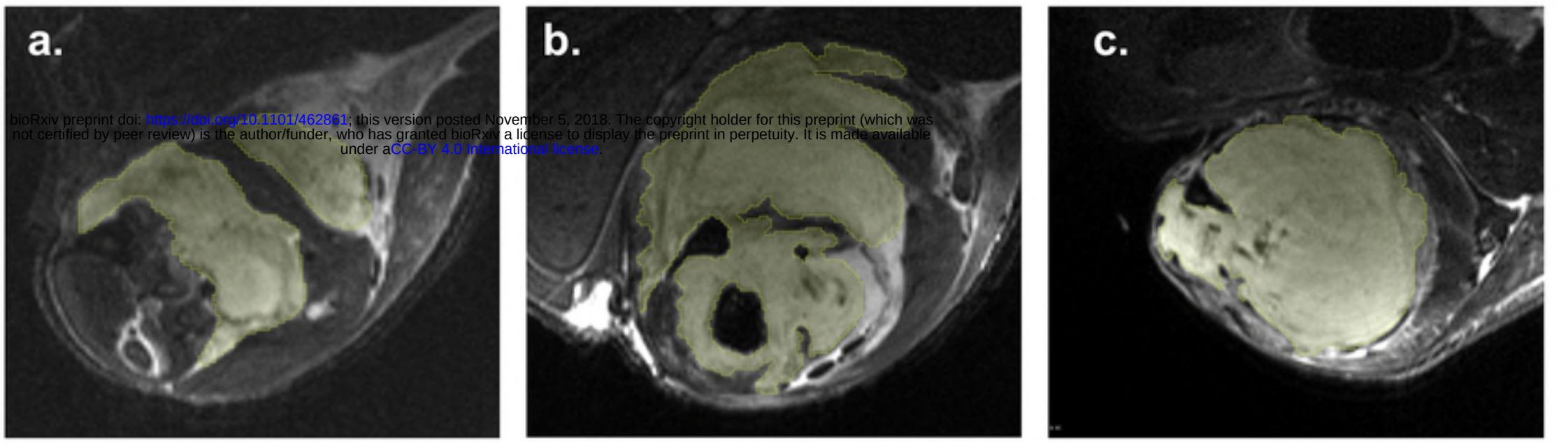

C.

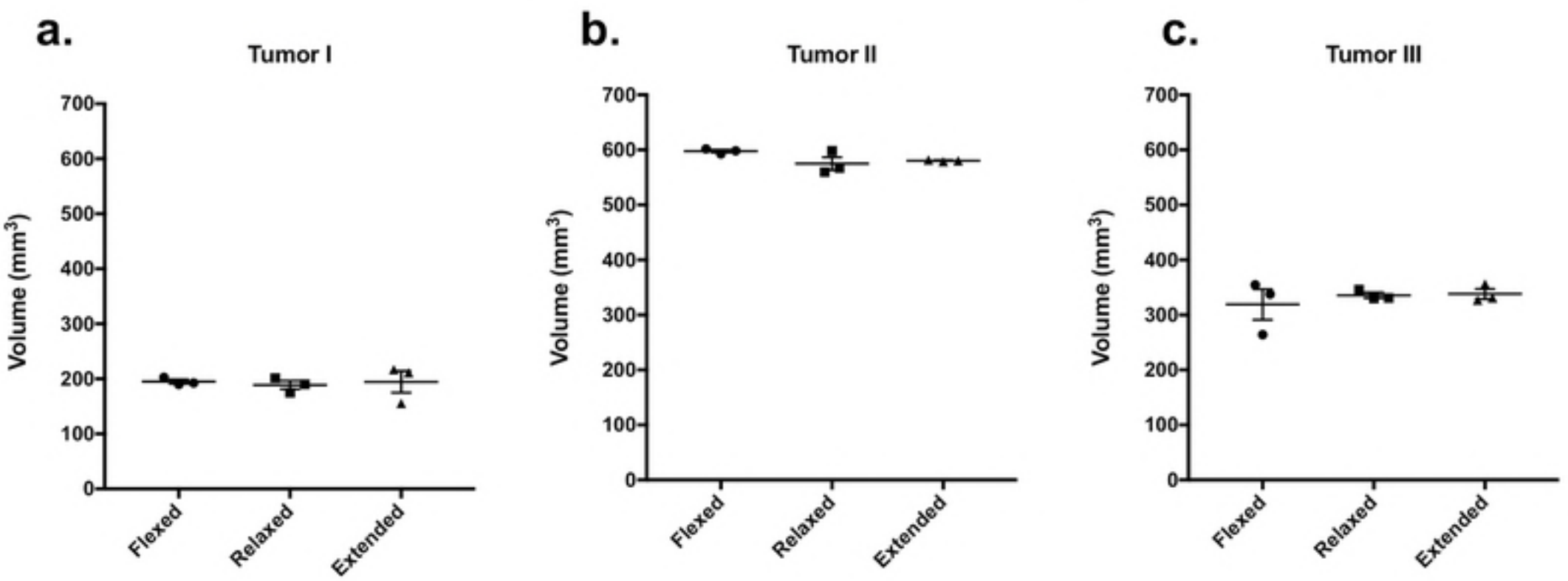

D.

Reproducibility of repeated scans
(One-way ANOVA analysis)

	F	p	r^2	Significant difference between means
Tumor I	0.752	0.9284	0.02445	ns
Tumor II	2.838	0.1357	0.4861	ns
Tumor III	0.366	0.708	0.1087	ns

E.

Precision of repeated measures
(Brown-Forsythe test)

F	p	Significant difference in SD
0.6131	0.5724	ns
1.327	0.3334	ns
0.9043	0.4537	ns

Fig 6

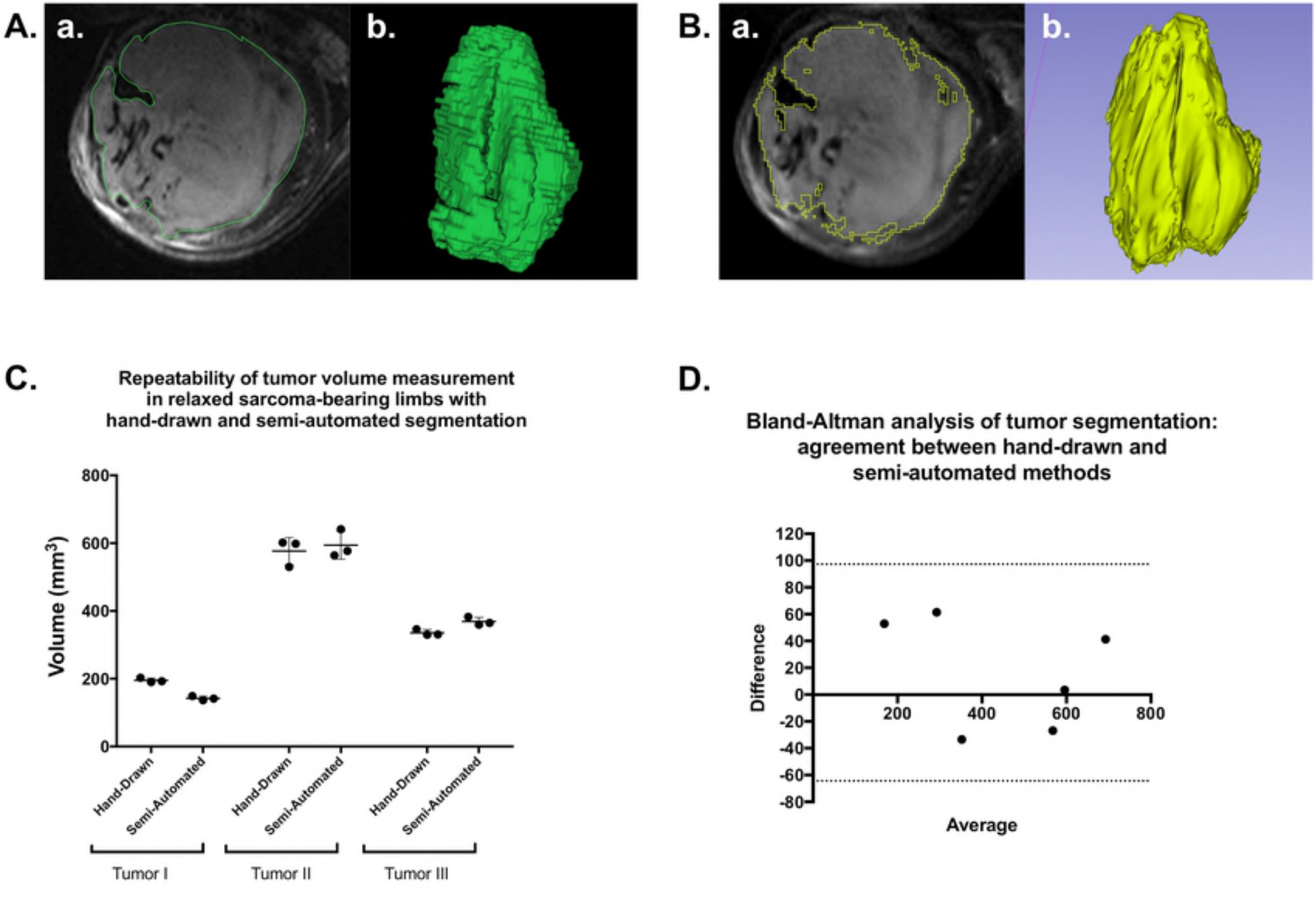
A.
a.
b.
B.
a.
b.
C.
Repeatability of tumor volume measurement
in relaxed sarcoma-bearing limbs with
hand-drawn and semi-automated segmentation
Volume (mm3)
800
600
400
200
0
Hand-Drawn
Semi-Automated
Hand-Drawn
Semi-Automated
Hand-Drawn
Semi-Automated
Tumor I
Tumor II
Tumor III
D.
Bland-Altman analysis of tumor segmentation:
agreement between hand-drawn and
semi-automated methods
Difference
120
100
80
60
40
20
0
-20
-40
-60
-80
200
400
600
800
Average

Fig 7

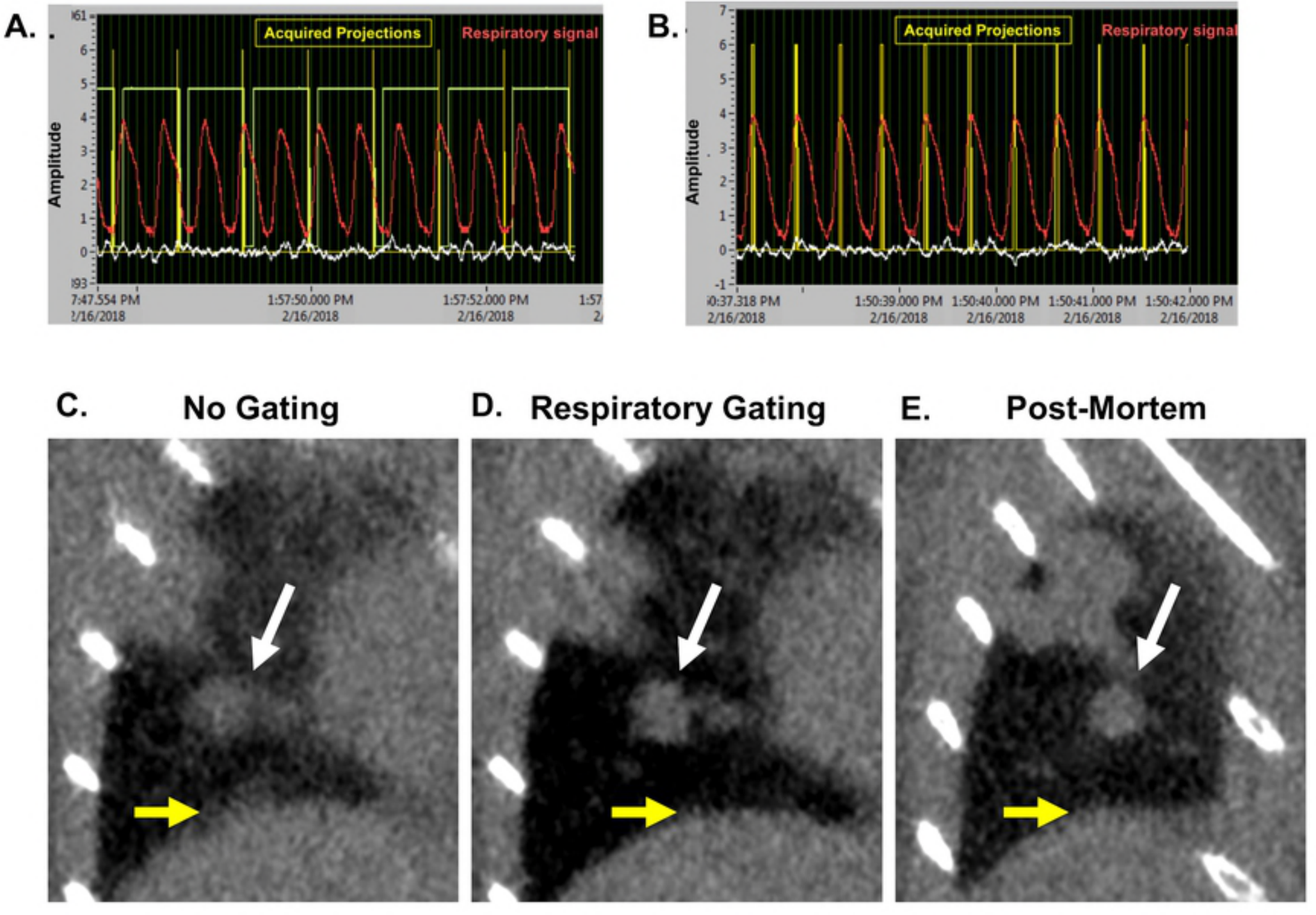
A.
Acquired Projections
Respiratory signal
Amplitude
7:47.554 PM
2/16/2018
1:57:50.000 PM
2/16/2018
1:57:52.000 PM
2/16/2018
B.
Acquired Projections
Respiratory signal
Amplitude
0:37.318 PM
2/16/2018
1:50:39.000 PM
2/16/2018
1:50:40.000 PM
2/16/2018
1:50:41.000 PM
2/16/2018
1:50:42.000 PM
2/16/2018
C. No Gating
D. Respiratory Gating
E. Post-Mortem

Fig 8

A.

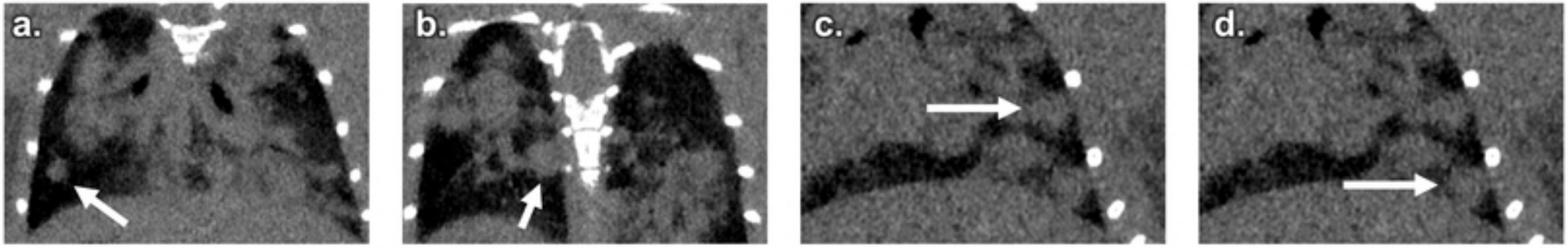

B.

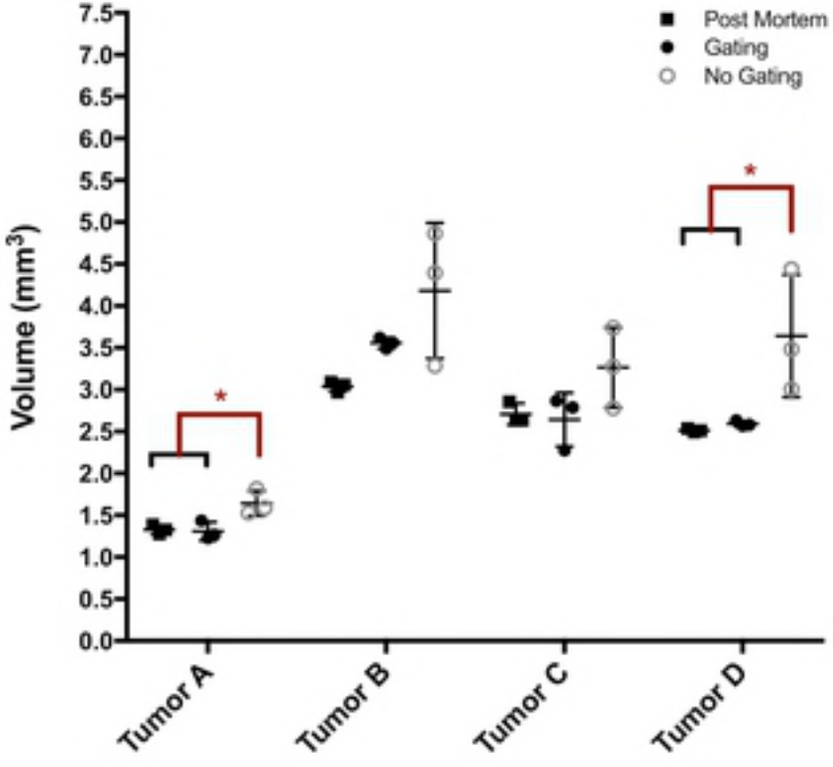

C.

Analysis of variance in lung tumor analysis with uCT

(One-way ANOVA analysis)

	F	p	r^2	Significant
Tumor A	8.362	0.0184	0.736	*
Tumor B	4.433	0.0658	0.5964	ns
Tumor C	2.992	0.1255	0.4994	ns
Tumor D	6.686	0.0297	0.6903	*

D.

Deviation and variance of repeated tumor volume measures in uCT

	Standard Deviation				Average Variance	Average coefficient of variance (%)
	Tumor A	Tumor B	Tumor C	Tumor D		
Post-Mortem	0.054	0.062	0.129	0.022	0.0060	2.94
Respiratory Gating	0.111	0.066	0.321	0.034	0.0302	5.94
No Gating	0.150	0.810	0.480	0.730	0.3603	15.81

Fig 9


Documents/Attachments
File Name
SOP - ParaVision 6.0.1 Operation and Simple Scan Setup.docx
SOP-Semi-automated tumor segmentation with ?GrowCut? in 3D Slicer.docx
CIVM Image Management: Tumor Growth Rate
All Studies
Current Study
Tumor Growth Rate
Parent Study
Preliminary U24
Datasets
List Datasets
Gallery View
List Structures
Upload
QA/Admin
Documents
Forms
Study Admin
User Admin
Groups Admin
Help
Search
Report Issue
Log Out
Thumbnail
Name
Description
Stacks
ID
Scan Date
Today
180420-1 B20027 T2W
Scan Day 2 (one week after initial scans) of control mice be...
3
14717
2018-04-27
Stacks (3)
Documents (add) (1)
Description
File Name
File Size
Dataset
Acquisition Report Day 2
Acquisition Report 180420-1 T2 Day 2
717.72 KB
180420-1 B20027 T2W
Add a new document
180420-1 B20027 T1W+Contrast
Scan Day 2 (one week after initial scans) of control mice be...
3
14716
2018-04-27
14717: 180420-1 B20027 T2W
Return to Previous Results
Download
as DICOM Stack (original format) [9 MB]
unknown sequence
71%
30/60
CIVM Image Management: U24 CT Lung
All Studies
Current Study
U24 CT Lung
Parent Study
Preliminary U24
Datasets
List Datasets
Gallery View
List Structures
Upload
QA/Admin
Documents
Saved Views
Forms
Study Admin
User Admin
Groups Admin
Help
Search
Report Issue
Log Out
Thumbnail
Name
Description
Stacks
ID
Scan Date
Today
IM-0001-0250.dcm
mouse / sarcoma
3
14725
2018-04-24
IM-0001-0250.dcm
mouse / Lung Tumors Gating
3
14724
2018-04-24
select/unselect all
Upload a Dataset
Move Selected Datasets
Go
14717: 180420-1 B20027 T2W
Return to Previous Results
Download
as DICOM Stack (original format) [9 MB]
unknown sequence
Generic Acquisition Report
Tumor Segmentation

Fig 10